COMPARISON OF LINEAR AND NONLINEAR NAVIGATION STRATEGIES FOR A EUROPA LANDER CONCEPT

Rohan Patel[*†] and Sonia Hernandez[*‡]

Navigation strategies typically use linearized techniques to predict maneuver statistics. This method has been successfully employed on numerous high-energy trajectories, but may not be valid for low-energy ones due to the highly nonlinear environment. We explore nonlinear navigation techniques applied to a Europa Lander concept by assessing trajectory sensitivity. The linearity assumption is tested at different phases of the endgame trajectory. Maneuver strategies and placement are considered to improve the delivery to Europa. Nonlinear statistical maneuver Monte Carlo simulations are conducted to optimize maneuvers and compare ΔV statistics against conventional linear simulations.

INTRODUCTION

Linear navigation techniques have been, and continue to be, successfully employed on various missions such as Cassini,[1,2] Juno,[3] and Europa Clipper.[4] High energy trajectories can utilize these techniques since the true dynamics of the trajectory can be sufficiently approximated by linearization about the reference trajectory. Low-energy trajectories, such as those used to explore planetary moons, are highly nonlinear and can be sensitive to state perturbations. In this paper we investigate the navigation of several low-energy approach trajectories to Europa by assessing trajectory sensitivity, and compare conventional Monte Carlo linear navigation techniques to nonlinear ones.

Europa has the potential to harbor life due to its subsurface ocean. Currently, the Europa Clipper orbiter is in development to study the Galilean satellite, but taking in situ measurements from the surface can help search for biosignatures. In order to land on the surface of Europa, a low-energy arrival needs to be considered as a conventional two-body (high-energy) approach would require significant ΔV. The interplanetary trajectory utilizes resonant transfers of the Galilean satellites to capture and pump down the orbit.[5] Eventually, the L_2 gateway serves as a natural access point to capture and land on the surface.[6]

The work presented here focuses solely on the "endgame" portion of the trajectory, which includes the last resonant transfer with Europa, entering through the L_2 Lagrange point, and landing on the surface. Several trajectory examples are considered; the generation of these are discussed further in the paper. The linearity assumption is tested for different portions of the endgame trajectory by comparing how error samples around each reference trajectory behave when propagating them using a linear approach (via the state transition matrix (STM)) versus a nonlinear approach (using full dynamics).

[*]Mission Design and Navigation Section, Jet Propulsion Laboratory, California Institute of Technology, 4800 Oak Grove Dr., Pasadena, CA, 91109
[†]Intern, Email: Rohan.Patel-1@colorado.edu
[‡]Mission Design Engineer, Email: Sonia.Hernandez-Doran@jpl.nasa.gov

The outline of the paper is as follows. The next section details the generation of five trajectory examples used during our analysis. The trajectories are initially generated in the Circular Restricted Three Body Problem (CR3BP) and then converged into a full ephemeris model. The next section assesses the linearity assumption for the five trajectory cases considered, by comparing the propagation of linear and nonlinear samples. A sensitivity to covariance scaling is conducted and suggestions for maneuver placement are discussed. Techniques to improve the delivery accuracy at Europa are considered in the next section. Linear and nonlinear Monte Carlo maneuver simulations are compared and each case is further optimized for ΔV in the next section. Lastly, we discuss concluding remarks and future work.

TRAJECTORY CASES

Survey and Generation

This work utilizes several full ephemeris trajectories computed from Reference 7. These cases were initially generated from a survey of approach trajectories in the CR3BP.[8] A grid of accessible and pragmatically feasible latitude and longitude coordinates were selected with an approach (landing) altitude of 50 km. Trajectories were constrained to a 0° flight path angle at this point, and the resulting state was backward propagated to the y-axis crossing, outside the radius of Europa's orbit, in the Jupiter-Europa rotating frame. Ultimately, candidates were narrowed down by Jacobi constant, between C= 3.0015-3.0030, from prior studies.[9] Cases with a resonance period with respect to Europa of 5:6 were kept to match the nominal baseline capture and pump-down trajectory.[5,6] Arrivals with latitudes greater than 50° were filtered out due to large deterministic ΔV requirements.[7] Finally, considerations for radiation exposure were made by limiting the flight time in L_1 and L_2 neck regions.

Selected Cases

Five candidate endgame trajectories were selected from the CR3BP survey for their navigation complexity and variation in approach. All candidates were propagated in full ephemeris using JPL's MONTE Software[*]. Figures 1 and 2 present each endgame case in the Jupiter-Europa rotating frame. The left-hand side sub-figure shows the resonant orbit of each trajectory which will be
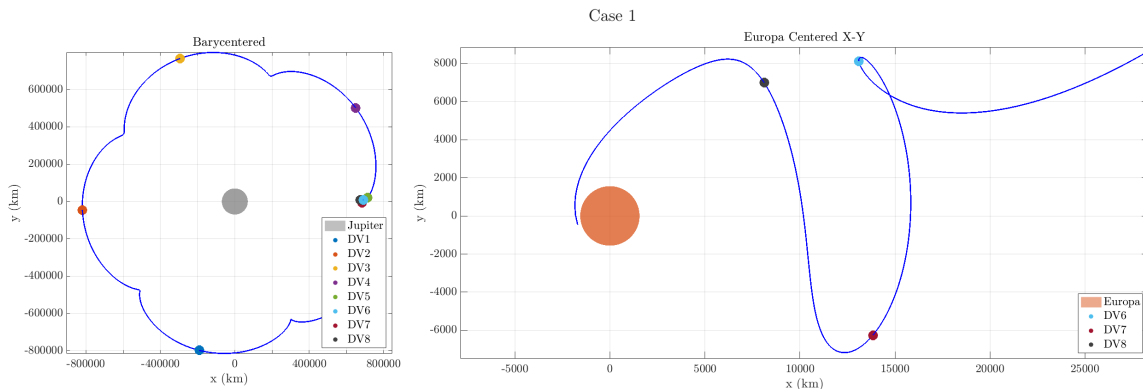

Figure 1: Case 1 approach trajectory to Europa with an arrival epoch of 27-MAY-2032 ET
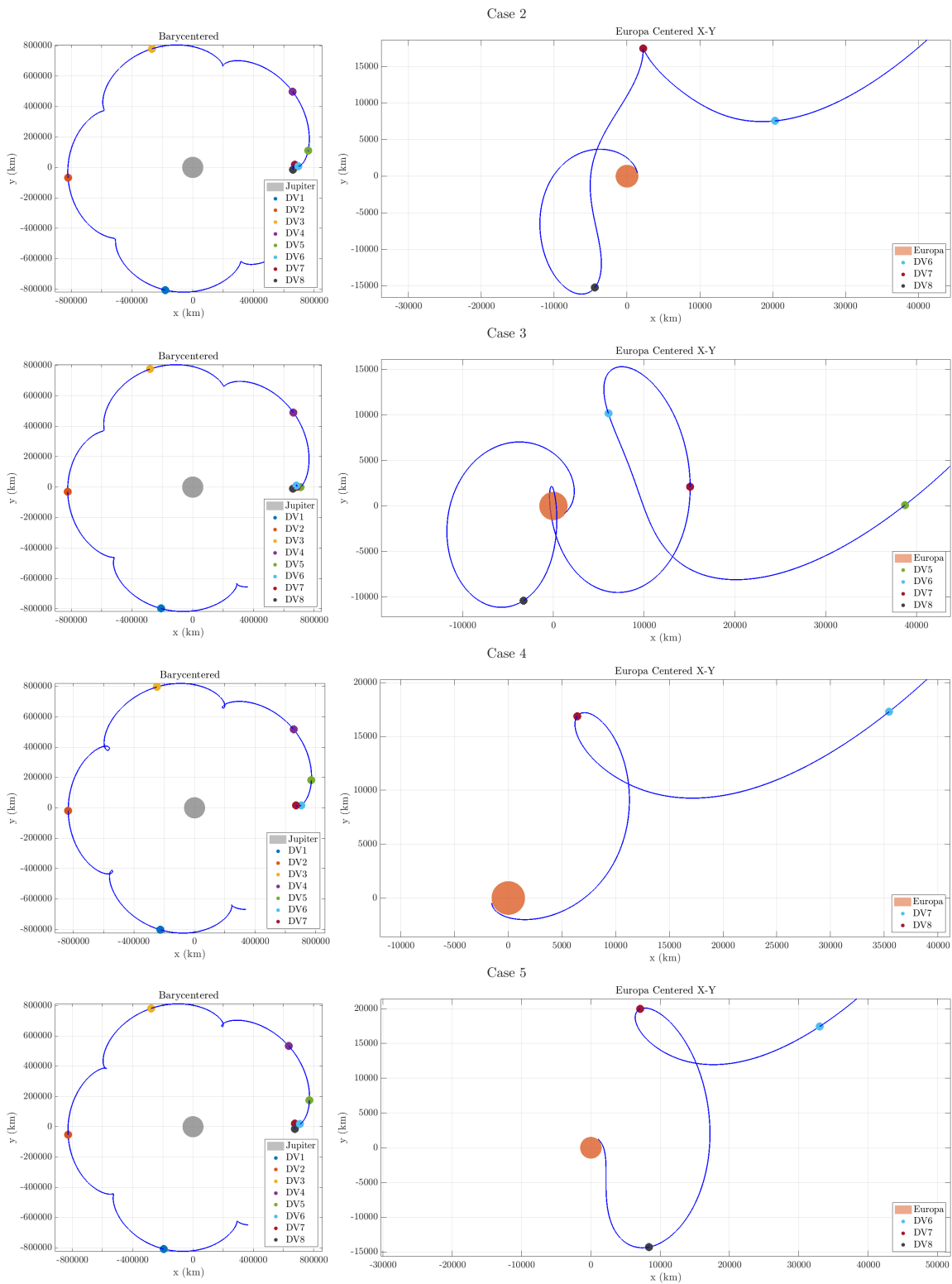
Figure 2: Cases 2-5 approach trajectories to Europa with a fixed 18-MAR-2031 ET arrival

referred to as the "resonant orbit" portion of the endgame. The right-hand side sub-figure is of the approach to Europa, referred to as the "final approach." The trajectories presented in this work are entirely ballistic assuming no prior state or maneuver execution errors. An optional Europa Orbital Insertion (EOI) or Deorbit, Descent, and Landing (DDL) deterministic burn could be placed at the arrival (end of the trajectory), but is not covered in this work. Statistical maneuver locations are shown in the both figures, and their location and magnitudes will be discussed further in the paper. Note that all cases presented are not planar restricted and have variation in their respective Z components. All candidate trajectories enter anti-Jovian via the L_2 neck region.

Case 1, seen in Figure 1, enters a Lissajous orbit around the L_2 point to a landing manifold. The full Lissajous revolution could be completed before landing as a staging-orbit if desired.[6] Case 2 follows a distant prograde orbit (DPO) past L_2 and then loops around L_1 for a retrograde landing. Case 3 also loops around the L_2 region and has a close approach to Europa before arriving retrograde on the sub-Jovian side. Because this case does not follow a conventional low-energy family, a unique name "AL-Retrograde" is assigned. Cases 4 and 5 are similar to the first case, but the loop is larger (since they are arriving at a higher energy) allowing for longer time spent near apoapsis before approach. Case 4 arrives on the sub-Jovian side of Europa while Case 5 arrives on the anti-Jovian side. Since Case 4 is a fast approaching trajectory, there is one less statistical maneuver than in the rest of the cases. Table 1 shows the time between statistical maneuvers and the deterministic ΔV for each case. Note, the Δt column of the last row for each case represents the time between the last maneuver and arrival at Europa.

Table 1: Reference trajectory time between maneuvers and deterministic ΔV.

Case	Case 1 L_2**Liss Prograde**		Case 2 **DPO-Retrograde**		Case 3 **AL-Retrograde**		Case 4 **1 Loop-Retrograde**		Case 5 L_2**Liss Prograde**	
Burn	Δt	Det. ΔV (m/s)	Δt	Det. ΔV (m/s)	Δt	Det. ΔV (m/s)	Δt	Det. ΔV (m/s)	Δt	Det. ΔV (m/s)
ΔV_1	4.27 d	0.000	4.27 d	0.000	4.27 d	0.000	4.27 d	0.000	4.29 d	0.000
ΔV_2	4.28 d	0.000	4.35 d	0.000	4.28 d	0.000	4.27 d	0.000	4.28 d	0.000
ΔV_3	4.29 d	0.002	4.18 d	0.000	4.29 d	0.000	4.14 d	0.000	4.11 d	0.000
ΔV_4	1.63 d	0.001	1.03 d	0.000	1.63 d	0.000	21.18 h	0.000	22.26 h	0.000
ΔV_5	20.0 h	0.001	20.0 h	0.000	20.0 h	0.000	20.00 h	0.000	20.0 h	0.000
ΔV_6	22.0 h	0.040	20.0 h	0.000	20.0 h	0.000	20.00 h	0.000	20.0 h	0.000
ΔV_7	20.0 h	0.010	22.0 h	0.003	22.0 h	0.008	20.00 h	0.001	1.08 d	0.000
ΔV_8	10.0 h	0.09	20.0 h	0.024	20.0 h	0.025	-	-	10.0 h	0.056

ASSESSING TRAJECTORY SENSITIVITY AND THE LINEARITY ASSUMPTION

Method

The navigation process consists of orbit determination (OD) and maneuver design (flight path control). OD utilizes observed measurements and the theoretical dynamics to generate the state of the spacecraft at a given epoch. This information is then used by the flight path control team to design maneuvers to reach a desired target (aimpoint). Deviations in state from the reference trajectory can be propagated forward in time to analyze the delivery errors to the aimpoint. Commonly, the nonlinear equations of motion for the spacecraft can be linearized around a nominal trajectory.[10] An initial state ($\vec{X}_i$) at epoch t_i along the reference can be mapped to a final state ($\vec{X}_j$) at epoch t_j given the state transition matrix (STM). Deviations from the nominal trajectory ($\vec{X}^*$) , denoted by $\vec{x} = \vec{X} - \vec{X}^*$, are mapped in time with the STM (Φ) in the following equation:

$$\vec{x_j} = \vec{x}(t_j) = \Phi(t_j, t_i)\vec{x}(t_i) = \Phi(t_j, t_i)\vec{x_i} \tag{1}$$

where $\Phi(t_i, t_j) = \frac{\partial \vec{X_j}}{\partial \vec{X_i}}$ (see Figure 3). Similarly, covariance (P) can be propagated using the STM as shown in Eq. (2). A covariance of state errors at a given epoch can be used to generate sample deviations.

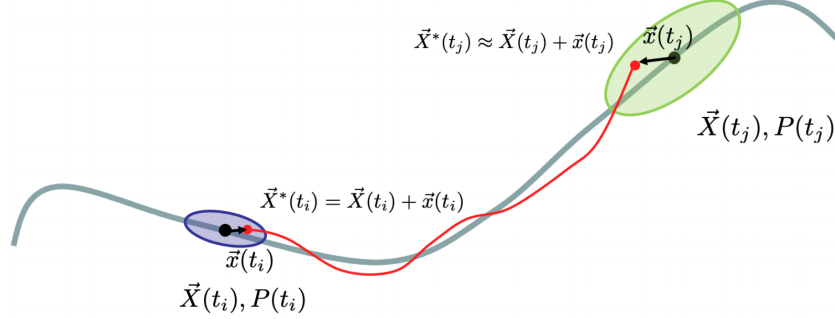$$P(t_j) = \Phi(t_j, t_i)P(t_i)\Phi^T(t_j, t_i) \tag{2}$$

Figure 3: Example of state ($\vec{X_i^*}$) with deviation $\vec{x}(t_i)$ mapped at time t_j to state ($\vec{X_j^*}$) with deviation $\vec{x}(t_j)$ and (P_j) using the STM. Similarly, a covariance (P_i) is mapped to (P_j) using Eq. (2).

As the nonlinearity of the dynamics increases, the true final state or covariance cannot be accurately captured by the linearity assumption, thus nonlinear propagation is required. This needs to be evaluated on a trajectory to trajectory basis as well as between certain epochs within a trajectory. This assumption can be studied by creating state deviations around a reference trajectory using a covariance, and then propagating them using both the STM and a full nonlinear propagation. If the linear and nonlinear resulting deviations have similar distributions (and not just aggregate statistics), then the linear method can represent the true dynamics of the system. This method does not take into account optimization to reduce errors to the target. The nonlinear propagator used in this work utilizes an N-body force model for gravitational forces and includes solar pressure. Included gravitational forces come from the Jovian satellites, Jupiter, and the Sun.

For the following trajectory sensitivity analysis, we will first remove correlation in variables unaffected by the dynamics of the system (i.e., observation errors and consider parameters). Deviations to the trajectory are due to prior state errors and maneuver execution only. Typically, the navigation process introduces these errors through an injection covariance matrix which is a result from launch vehicle trajectory's errors. In planning, this matrix is estimated, as the true covariance will only be known once the actual mission is flown. Simulated errors are then propagated, and statistical maneuvers are designed to get the spacecraft back to the nominal state. This process yields updated covariance matrices in time. Using an injection covariance and propagating the trajectory all the way to the endgame segment is computationally expensive. Therefore, a covariance matrix is generated from prior statistical maneuver simulations which were examined in Reference 7. The covariance can be scaled by a multiplier to create larger or smaller deviations for this analysis.

Throughout the paper, the radial and position differences are used to compare sample deviations to the reference trajectory. The radial error, Δr, is defined as the difference between the radii of the sample and the reference (Eq. 3). This equation is essential to understand the altitude difference of the sample at arrival, after subtracting the radius of Europa. Δr is different than Δp, referred to here as the position error, which accounts for the latitude, longitude, as well as the radius (Eq. 4). The velocity difference (Δv) is computed identically to Δp, but for the states' velocity vector. This should not be mistaken for ΔV which denotes the magnitude of a burn.

$$\Delta r = ||\vec{X_s}|| - ||\vec{X_{ref}}|| \tag{3}$$

$$\Delta p = ||\vec{X_s} - \vec{X_{ref}}|| = ||\vec{x}(t)|| \tag{4}$$

It is anticipated that the linearity assumption will be valid throughout the resonant orbit approach to Europa for a considerable time duration. Linear propagation of resonant trajectories have been previously employed successfully,[1,4,11] and its application to the candidate cases is show. Roughly two days from arrival, the trajectory becomes significantly nonlinear. Therefore, a separate analysis for this portion of the trajectories considered is conducted.

Resonant Orbit

Figure 4 shows resulting deviations from the reference state for Case 1 (Figure 1) with a propagation start immediately after ΔV_2 (left sub-plot) and ΔV_3 (right sub-plot) up to the ΔV_4 epoch. After roughly four and eight days of propagation respectively, the linear samples (blue) map similarly to the nonlinear samples (red). Using linear propagation in this portion of the trajectory appears to sufficiently represent the dynamics of the system, and can be utilized for statistical maneuver planning and simulations. Note that errors are large for the ΔV_2 to ΔV_4 example as this does not include ΔV_3's execution. Because all cases follow a similar approach resonance to the endgame portion of the trajectory, the distributions of errors for Cases 2-5 will be similar to that of Case 1. Table 2 shows difference between the nonlinear and linear results: mean, 99th percentile, and maximum error for all cases from ΔV_3 to ΔV_4.

Table 2: Difference between nonlinear and linear Δp error for propagation from ΔV_3 to ΔV_4.

	Case 1	Case 2	Case 3	Case 4	Case 5
	L_2Liss-Prograde	DPO-Retrograde	AL-Retrograde	1 Loop-Retrograde	L_2Liss-Prograde
Δ Mean (km)	3.47	2.45	0.74	4.36	0.70
Δ $99^{th}\%$ (km)	9.73	16.59	3.66	30.22	5.43

Final Approach Trajectory

During the final approach phase to Europa, each trajectory becomes much more sensitive to variation in the initial conditions. To assess how sensitive each trajectory is, two test cases are conducted: 1) fixed initial dispersion mean at 48 hours to arrival and 2) sensitivity to covariance scaling at 20 hours to arrival. Statistical maneuver placement for the following cases has been completed previously in Reference 7. Maneuvers were placed by considering the apoapsis location and the time to arrival. 20 hours between maneuvers is considered to be sufficient to update spacecraft knowledge, create an maneuver plan, and send this to the spacecraft.[7] Maneuvers 10 hours before arrival are
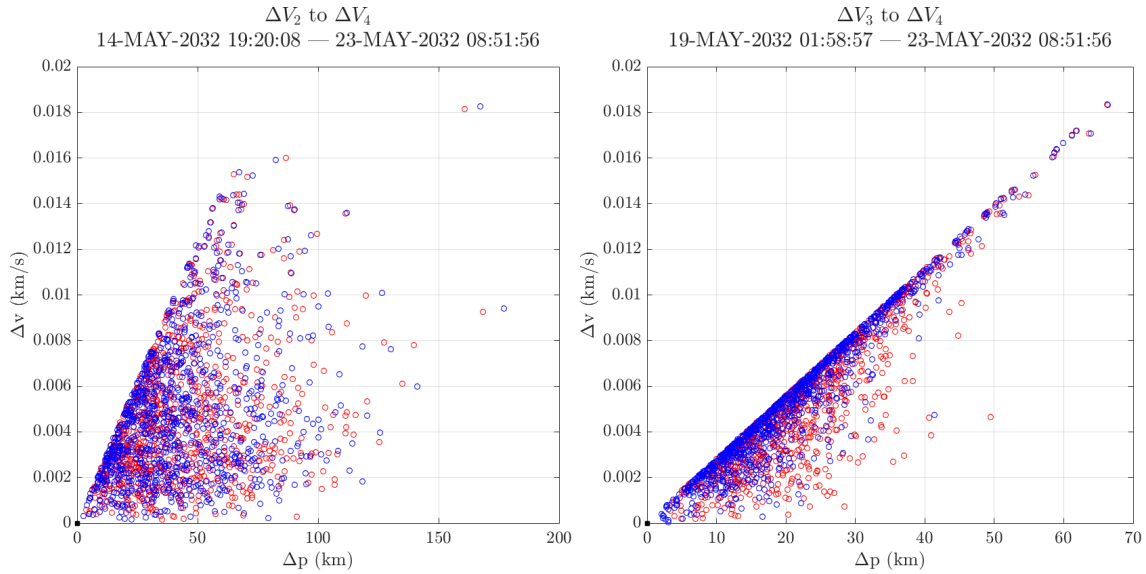
Figure 4: Case 1 linear (blue) and nonlinear (red) samples' deviation at the ΔV_4 epoch.

included as an option as well since this would be enough time for a DDL command to be updated for an accurate landing. Cases 1 and 5 include such burn, and all cases abide by the 20 hour spacing between burns. By using prior simulations as a starting point, an accurate dispersion covariance can be created and propagated to an arbitrary start time. This is possible as the previous work demonstrated that maneuver to maneuver targeting, as opposed to targeting all maneuvers to arrival, can make the linear assumption usable. We now show that if the propagation time is too long, or the dynamics become highly nonlinear, the linearly propagated samples do not accurately represent the dynamics of the system and either method yields large errors downstream if uncorrected by additional statistical maneuvers. Through the rest of the paper, we cover all the trajectories at a high level, and include further analysis for Cases 3 and 5. Case 3 includes a close approach to Europa before landing, which makes the navigation unique compared to the other candidates. Case 5 is selected as it follows the same approach as the baseline (Case 1), but with improved overall performance.

Table 3: Position error statistics at the arrival target. Propagation begins 48 hours prior to arrival with an initial mean position error of roughly 1 km.

Case	Covariance Scale	Initial Position			Δp Nonlinear			Δp Linear		
		mean	1-σ	99%	mean	1-σ	99%	mean	1-σ	99%
		(km)	(km)	(km)	(km)	(km)	(km)	(km)	(km)	(km)
1	0.06	0.99	0.72	3.19	41.32	31.83	134.54	41.30	31.86	135.14
2	0.50	1.04	0.60	2.94	170.74	119.70	528.81	171.04	120.21	532.02
3	0.06	0.99	0.74	3.35	64.05	49.29	212.95	64.05	49.30	213.08
4	0.33	1.06	0.51	2.56	20.26	15.97	70.07	20.24	15.97	69.32
5	0.25	1.11	0.73	3.54	16.65	12.40	52.41	16.64	12.41	52.41.

Table 3 summarizes resulting position errors for the linear and nonlinear propagation 48 hours from arrival assuming no additional burn is performed. The initial covariance is adjusted using the

scaling factor to make the mean position error at the start roughly one kilometer. The mean, standard deviation (1-σ), and 99th percentiles are included for each trajectory's initial time and the arrival is propagated in a nonlinear and linear fashion. For all cases, the 1-σ value before propagation is under 1 km and the greatest 99th percentile value is 3.54 km occurring in Case 5. At arrival, both the linear and nonlinear mean and standard deviation show large deviations from the reference trajectory making all cases infeasible if a maneuver cannot be performed within 48 hours to arrival. Case 2, the DPO to L_1 loop trajectory, has the largest error with a 1-σ and 99th percentile values at 119.70 and 528.81 km, respectively. Note that Case 2 requires a larger scaling compared to the other cases to achieve a 1.04 km mean position error, because the apoapsis of the orbit is located roughly 48 hours to arrival (as seen in the previous subsection, state errors minimize at apoapsis). Case 1 has the smallest covariance scaling at only 5.5% and it still has a delivery error standard deviation of 31.86 km. Despite Case 5 having the greatest variance in its initial position, it performs best with the smallest error, but is still considerably large with a mean of 16.64 km. As shown, each candidate trajectory is very sensitive to initial conditions. Unlike the resonant orbit portion, the final approach will require frequent statistical maneuvers to correct state errors until the delivery to Europa.

Figure 5 visualizes the state errors in time from Table 3 for Case 3. The initial dispersion covariance comes from ΔV_6 which occurs 14 hours before the starting point in the figure (48 hours before arrival). From around hours 17 to 25 from the starting point, both the position and velocity errors increase nonlinearly, reaching a maximum peak at the Europa periapsis. Placing a maneuver at this point would yield significant initial state errors, thus resulting in larger maneuver ΔVs. Also, if a maneuver is placed at periapsis, insufficient time is available from this point to arrival to correct any errors that have accumulated due to the 20 hour constraint. Therefore, statistical maneuvers in general should be placed well before or after periapsis. Currently, maneuvers ΔV_7 and ΔV_8 follow this condition and the time constraint. Maneuver ΔV_7 can be moved around by 2 hours as well and still meet the time constraint. Common across all the cases is errors growing exponentially near Europa. However, the extent to which they grow varies by case.
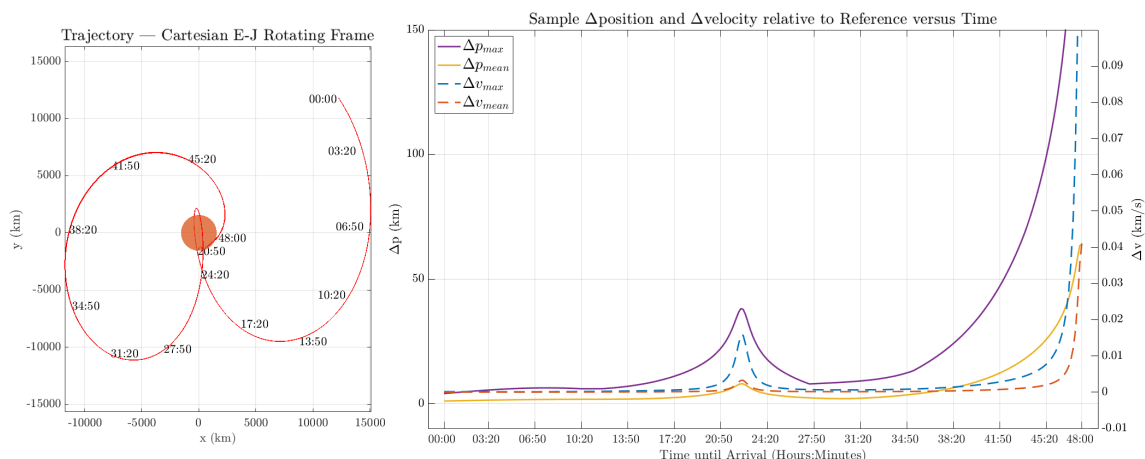

Figure 5: Case 3 - Propagation from 48 hours to arrival beginning with an initial covariance error of approximately 1 km.

Figure 6 shows linear and nonlinear samples for Case 3 mapped to cartesian coordinates in an inertial frame from ΔV_6 (a), ΔV_7 (b), and ΔV_8 (c) to arrival. The blue samples represent linear propagation, while the red ones represent nonlinear propagation. There is a clear discrepancy be-

tween the samples in (a), which is merely 2.5 days from arrival. As the propagation time reduces, the discrepancy between the samples also reduces. Figure (c), which is propagated 20 hours before arrival, shows that only at this point are linear and nonlinear samples behaved similarly. Recall that Table 3, propagated 48 hours before landing, shows that the linear and nonlinear propagation methods predict nearly the same mean, standard deviation, and 99th percentiles, despite having large errors at the arrival aimpoint. While the aggregate statistics are similar, the distributions of samples have considerable variation. For example, Figure 7 contains the delivery to arrival from ΔV_7 (top) and ΔV_8 (bottom) in the spherical IAU 2009 Europa fixed frame. The left subplots shows velocity vs. radius, the middle latitude vs. longitude, and the rightmost subplot flight path azimuth vs flight path angle. For the ΔV_7 to arrival propagation (44 hours), the latitude, longitude, flight path angle, and flight path azimuth distributions for the linear and nonlinear cases are roughly identical. However, from the velocity versus radius subplot, it is clear that the linear assumption does not accurately map the velocity. The "C" shape in the linear samples might seem counter intuitive, as the behavior looks nonlinear, but recall that these results are shown in a Europa rotating frame. Also from this subplot we can conclude that the lower the radius is, the velocity grows significantly, but as the radius increases the subsequent velocity does not decrease in a similar but opposite manner. For maneuver simulation optimization routines that rely on the linear assumption, this inconsistency can yield erroneous results if the propagation duration is too long. The behavior disappears when reducing the time to 20 hours as seen in the lower subplot. Here, the linear and nonlinear samples have similar resulting distributions.
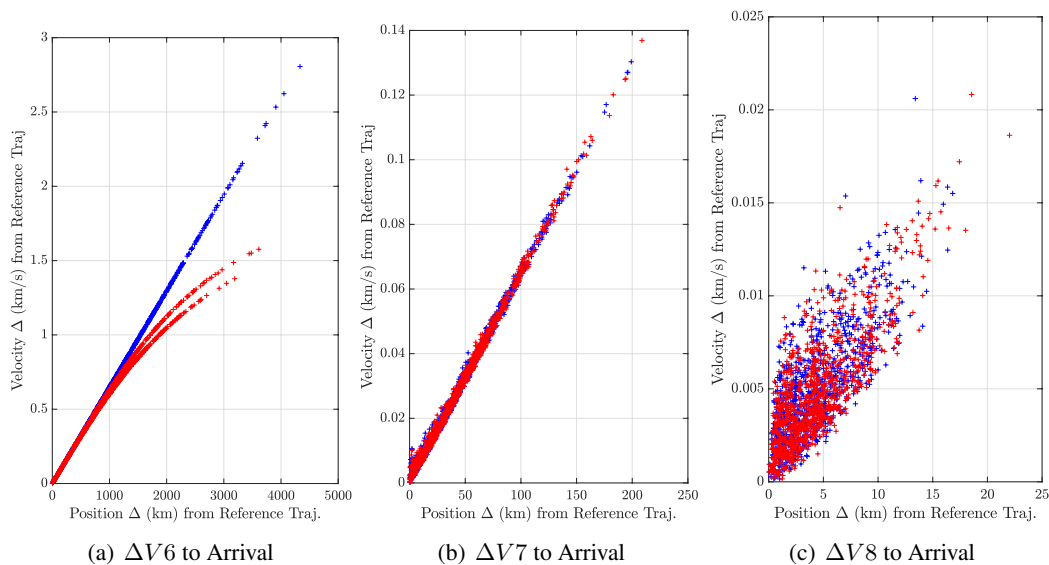

(a) $\Delta V6$ to Arrival   (b) $\Delta V7$ to Arrival   (c) $\Delta V8$ to Arrival

Figure 6: Case 3 - Resulting state dispersion from ΔV_6, ΔV_7, and ΔV_8 to arrival in an inertial EME2000 frame, for linear (blue) and nonlinear (red) sample propagation in a Δv vs. Δp plot. The reference arrival location is at the origin.

Case 5's approach from 48 hours before landing with a covariance scale of 0.25 is shown in Figure 8. At around 7 hours into the trajectory, errors reach a minim due to the apoapsis condition, and this is where ΔV_7 is placed. Another minimum occurs around 14 hours prior to landing, which is where ΔV_8 is located. Sample deltas diverge close to arrival, but not as significantly as seen in Case 3. Figure 9 shows the distribution of both cases from ΔV_7 and ΔV_8 to arrival. Like Case 3,
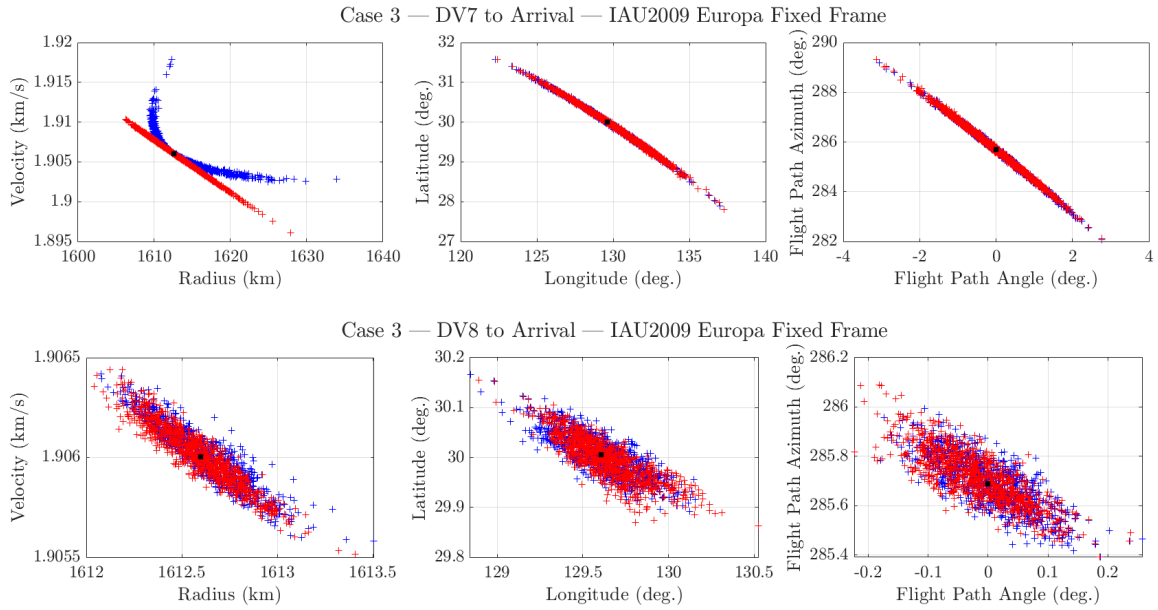
Figure 7: Case 3 - Resulting state dispersion from ΔV_7 and ΔV_8 to arrival for linear (blue) and nonlinear (red) propagation. The reference arrival location is the black square.

the velocity change is smaller at higher radii and is larger for lower radii for the linear samples (left subplot). The rest of the coordinates (middle and right subplot) have nearly identical distributions to their nonlinear counterparts. With ΔV_8 to arrival, the propagation time is reduced to only 10 hours which makes the linear samples accurately represent the dynamics of the system. It is also worth noting how the inclusion of ΔV_8 significantly improves the delivery to the aimpoint.
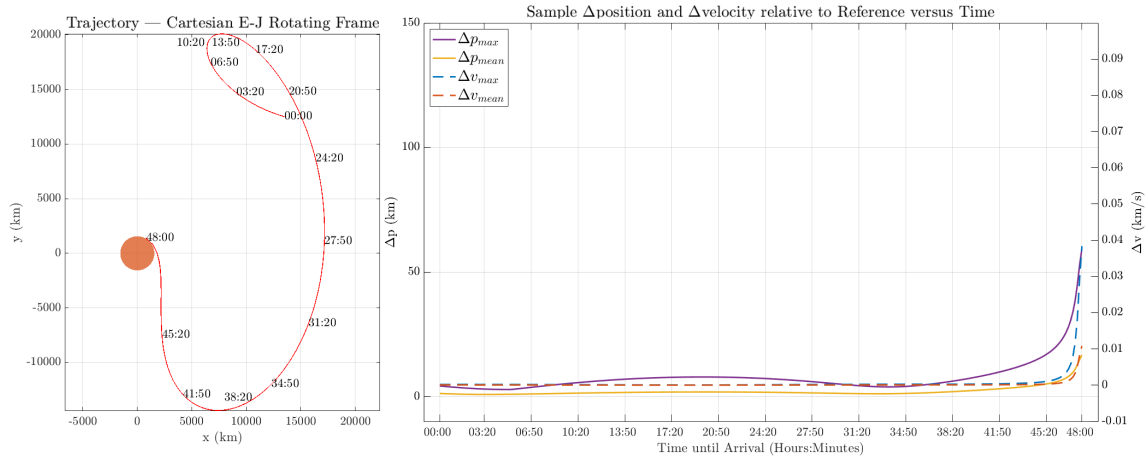
Figure 8: Case 5 - Propagation from 48 hours to arrival.

To assess sensitivity to covariance scaling, a second test was conducted on each trajectory by propagating 20 hours to arrival. The covariance scaling factor was varied from 0.05 to 1.4. The results are presented in Table 4. Case 2 has the smallest Δp of all the trajectories despite having the largest deviations from the 48 hours to arrival test. Recall that large deviations in the 48 hours
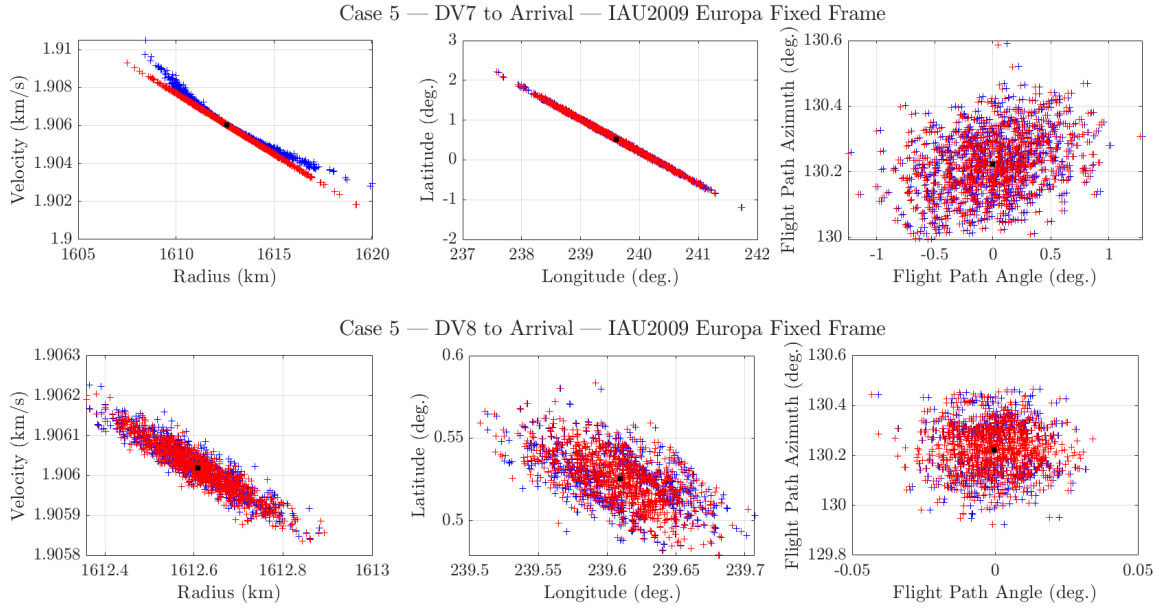
10

Figure 9: Case 5 - Resulting state dispersion from ΔV_7 and ΔV_8 to arrival for linear (blue) and non-linear (red) propagation. The reference arrival point is the black square.

to arrival test are only seen as a larger covariance scale was required to meet the one kilometer mean standard deviation due to errors reducing near apoapsis. Errors grow roughly linearly with increase in the covariance scaling factor. The linear samples have similar values to the nonlinear ones because the propagation duration is short enough. At 1.0 covariance scale, trajectories that performed all the statistical maneuvers have mean Δp values under 4.20 km. This potential error is still large enough to warrant exploring alternative navigation strategies to reduce errors at the delivery aimpoint.

Table 4: Samples propagated mean Δp (km) at arrival for varying covariance (20 hours to arrival). Cases 1 and 5 are omitted as ΔV_8 is not performed.

	Case 2 DPO-Retrograde		Case 3 AL-Retrograde		Case 4 1 Loop-Retrograde	
Cov.	Non-Lin.	Lin.	Non-Lin.	Lin.	Non-Lin.	Lin.
0.1	0.31	0.31	0.43	0.43	0.37	0.37
0.2	0.64	0.64	0.81	0.81	0.71	0.71
0.4	1.24	1.24	1.62	1.62	1.42	1.42
1.0	3.19	3.19	4.08	4.20	3.56	3.56
1.4	4.43	4.43	6.16	5.83	5.03	5.04

VARIABLE TIMING TO ARRIVAL

So far, all propagations have targeted a fixed arrival epochs. Modifications to the nonlinear propagator were made to include termination conditions. These include a fixed spherical flight path angle (FPA) and fixed radius to match the target arrival FPA or radius, respectively. The total propagation time was extended to account for samples reaching these events after the deterministic arrival epoch. The following cases start immediately after executing ΔV_8 which is the terminal maneuver before

arrival. No modifications to the burn magnitude is made implying that the cost of terminating to a condition different than the arrival epoch is the same as a fixed time case. In testing, samples that arrived above the target radius never reached the terminating condition so they were discarded. This means roughly half of the samples were omitted, making for an inaccurate data set. Similar behavior would occur if velocity, latitude, or longitude were searched for. The fixed condition was changed to flight path angle instead as this is also an important consideration for the DDL or EOI portion of the mission.
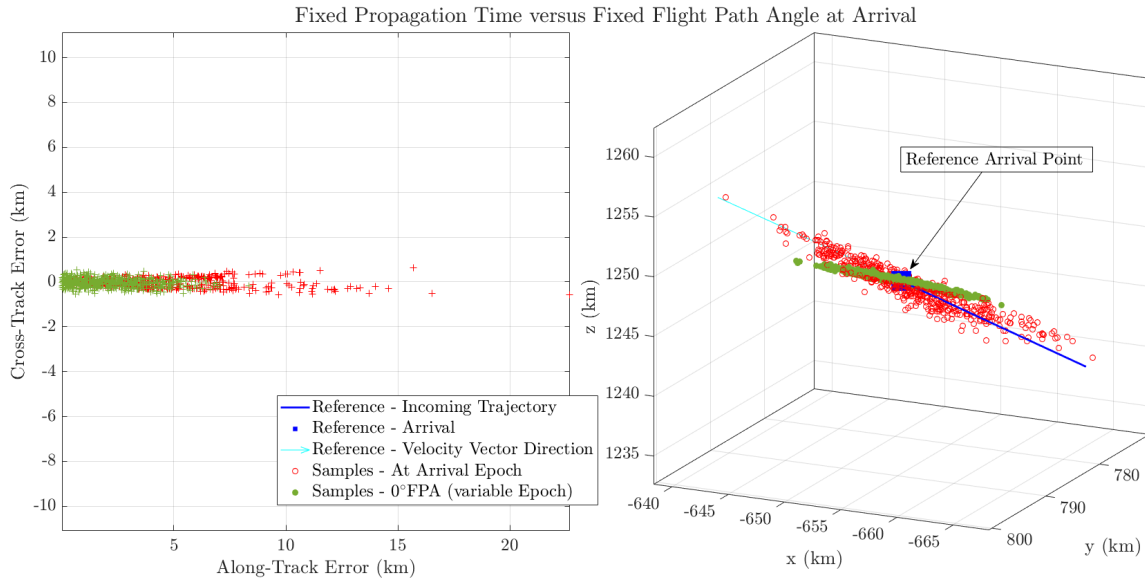

Figure 10: Case 3 errors at arrival shown in along and cross-track (left subplot) and EME2000 Cartesian (right subplot) for fixed propagation time samples (red) and fixed flight path angle samples (green).

Figure 10 shows Case 3's distribution of along-track versus cross-track error. The right subplot includes the incoming reference trajectory (blue line) and arrival location (blue square with annotation) in EME2000 Cartesian coordinates. Every other sample for the fixed propagation time (red) and fixed flight path angle (green) is plotted. The left subplot shows that the along-track error for fixed propagation can extend past 15 km while the cross-track is less than 1 km. By instead propagating to the arrival condition's flight path angle ($0.00°$ in this case), the along-track is reduced to under 10 km with a majority of samples being under 5 km. The cross-track error is still comparable to the fixed epoch time case. The landing epoch Δt mean, sigma, and 99th percentiles are: 0.0 seconds, 2.0 seconds, and 6.0 seconds respectively. Figure 11 plots the terminal state for the fixed epoch and FPA samples in spherical coordinates in the IAU 2009 Europa Fixed frame. The black square point represents the target aimpoint value. Both cases have similar radius and velocity magnitude distributions as seen in the left subplot. However, significant differences exist in the flight path azimuth, latitude, and longitudinal errors. The right subplot shows the flight path angle versus flight path azimuth. By the propagation termination condition, the FPA errors are reduced to zero, but an improvement in the flight path azimuth to the target can also be seen. The flight path azimuth 1-σ is reduced from $0.107°$ to $0.063°$. Also, a significant improvement to the latitude and slight improvement to the longitude at delivery is seen in the center subplot. The 1-σ for the fixed FPA samples is around 68 times smaller than the fixed epoch samples.

Figure 11: Case 3 propagated to fixed arrival epoch (red) versus fixed $0.00°$ flight path angle (green) nonlinear samples.
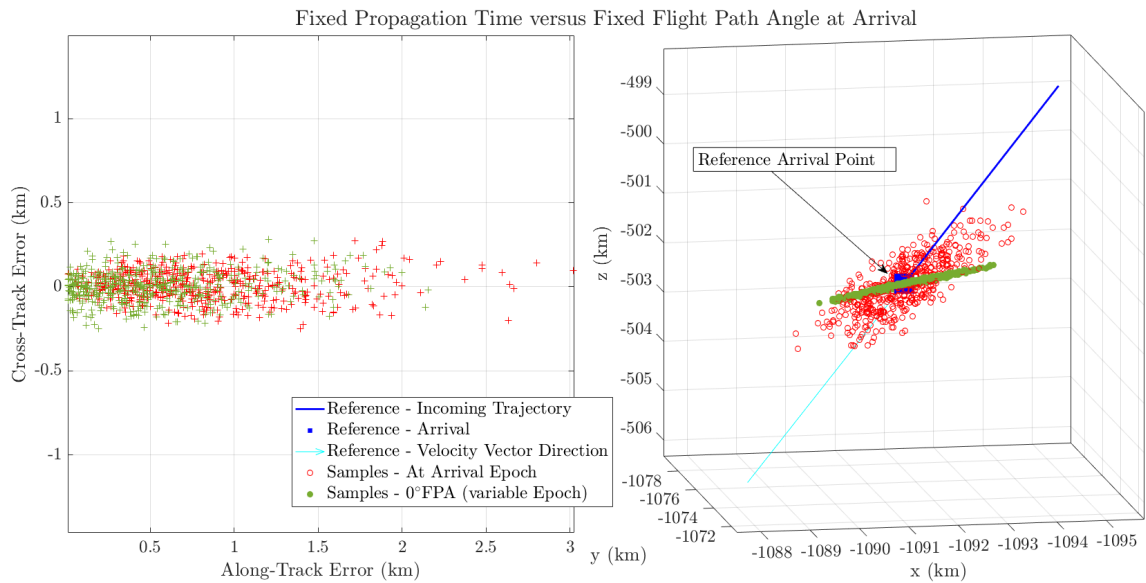
Figure 12: Case 5 errors at arrival shown in along and cross-track (left subplot) and EME2000 Cartesian (right subplot) for fixed propagation time samples (red) and fixed flight path angle samples (green).

Figure 12 shows Case 5's along-track and cross-track errors for the fixed FPA and fixed propagation epoch. Recall that this trajectory is less sensitive than all the previous cases. Therefore, the spread of the non-linear samples from ΔV_8 to arrival are smaller. In this case, the along-track standard deviation increases by 4.6 meters which is relatively small. The cross-track standard deviation decreases by 85 meters. Figure 13 compares the two propagation methods at their terminal conditions. Like Case 3, the radius and velocity distributions are nearly identical between the fixed

FPA and epoch runs. The latitude error is significantly decreased, but the longitudinal error and flight path azimuth are similar to the fixed epoch condition. This is because the Δt 99th percentile for the fixed FPA samples is less than one second mean there isn't enough time difference between the runs to make a significant difference. The fixed epoch samples are accurate, but the delivery to the target can be improved even more so by variable epoch, fixed FPA propagation.

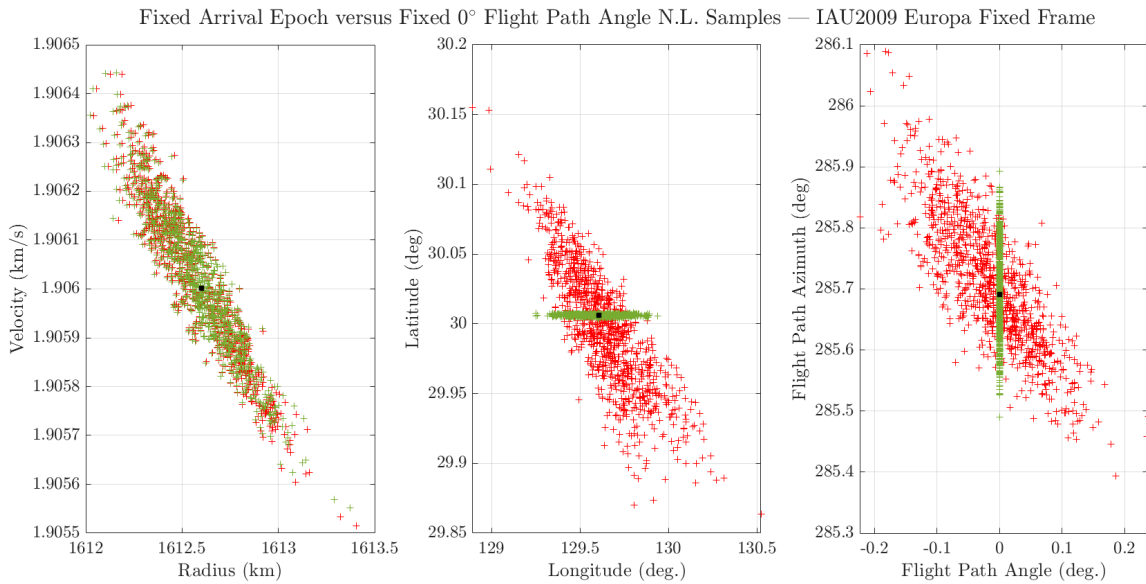**Figure 13**: Case 5 propagated to fixed arrival epoch (red) versus fixed $0°$ flight path angle (green) nonlinear samples.
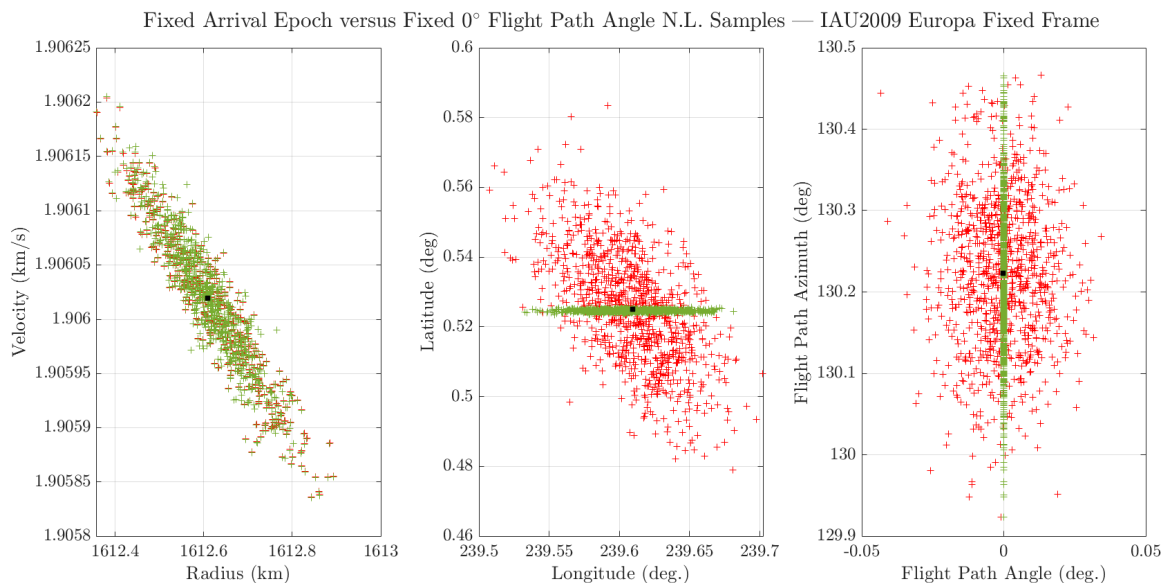
Because Case 5 uses a maneuver 10 hours from landing, an additional run was created to study the effects from ΔV_7 to arrival. This increases the propagation time to roughly 36 hours, and makes the distribution differences more apparent. Like Case 3, errors in radius and velocity are essentially unchanged. However, the latitude standard deviation decreased from $0.513°$ to $0.003°$ and the longitude decreased from $0.630°$ to $0.004°$. Both coordinates have mean values nearly identical to the deterministic point, implying the delivery errors for latitude and longitude are significantly reduced. Errors in flight path azimuth remain unchanged with standard deviations for the fixed FPA and epoch being $0.092°$ and $0.094°$ respectively. It is important to note that the Δt standard deviation and 99th percentile are relatively large at 11 seconds and 26 seconds. Changing the landing epoch can significantly improve the delivery to the target conditions. However, errors in radius and velocity are still similar to that of the fixed epoch propagation samples.

MONTE CARLO MANEUVER SIMULATION

Monte Carlo methods for maneuver analysis are commonly conducted to produce ΔV and subsequent delivery statistics.[10] The MONTE software suite includes a Linear Analysis of Maneuvers with Bounds and Inequality Constraints (LAMBIC) package that is used setup and run linearly propagated maneuver Monte Carlo simulations. A nonlinear counterpart, Casino, is also included in the suite and is used to create the following simulations. At a given epoch, error samples are introduced based on orbit determination knowledge, uncertainties in state, and maneuver execution to reach a target. Targets (also referred to as aimpoints) include a bounded position or velocity condition expressed in spherical, Cartesian, or B-Plane coordinates with a respective input frame. Optimization

of corrective ΔV's, to reach the desired aimpoint require an iterative search including propagation. This propagation can be done by linearizing the dynamics relative to the reference trajectory with the state transition matrix as seen in Eq. (1). The nonlinear method utilizes a multi-force model propagator instead, thereby altering how the ΔV is calculated. Maneuvers can act in chains with a common cost function to reduce the total ΔV across the set. Bounds can also be adjusted according to the sensitivity of the aimpoint for the mission to further reduce the required ΔV. Simulation products range from maneuver statistics, burn angles, mass decrements, and targeting errors for any specified number of samples. Commonly assessed variables include the mean, 1-sigma, and 99th percentiles for each maneuver magnitude. Their respective position, radial, and velocity errors are also analyzed to determine the delivery to the aimpoint.

Setup

Orbit determination knowledge is assumed to be perfect in the maneuver simulations conducted. Therefore, the sources of errors are in initial state and maneuver execution. State errors are generated at the simulation start time with an input initial covariance matrix. This matrix is generated from the baseline jovicentric pump-down trajectory for each case. For every linear and nonlinear Monte Carlo run, 5000 samples were generated for each maneuver. Execution errors for both are created using the Gates error model. This model consists of four error properties for an executed ΔV vector: the fixed and proportional, magnitude and directional errors.[11, 12] Table 5 summarizes the nominal Gates model setup used for all of the simulations. The values are either doubled or halved for a sensitivity to maneuver execution analysis summarized in Table 13. All cases were run and optimization without mass decrements. Target bounds and maneuver chains were investigated and the best run case is presented.

Table 5: Maneuver Execution Error Model Parameters

Nominal Gates Error Model Setup	
Fixed Magnitude 1-σ	4.669 mm/s
Fixed Pointing Error 1-σ	3.330 mm/s
Proportional Magnitude 1-σ	1.330 %
Proportional Pointing 1-σ	8.325 mrad

Comparing Linear and Nonlinear Monte Carlo Simulations

Cases 3 and 6 were simulated linearly and nonlinearly without optimization, or changing maneuver epochs, to evenly compare the two techniques. Maneuvers target the Cartesian position coordinates of the next maneuver state. The final maneuver targets the radius, latitude, and flight path angle, at the deterministic arrival epoch. Each run was set to create 5000 samples and the nominal gates error model was used. Table 6 outlines the maneuver and delivery statistics for Case 3. Across both runs, the total ΔV statistics are large, but this is attributed to being an unoptimized, fix bounds case. For the nonlinear run, a total of 30 samples (0.6% of the set) were discarded as these had disproportionate statistics with respect to the rest (the trajectory was unable to reach the arrival point). The linear results have a total mean, 1-σ, and 99th percentile of 12.44, 8.91, and 41.76 m/s respectively. The nonlinear results are similar but are always greater than the linear ΔVs with a total mean, 1-σ, and 99th percentile of 12.74, 9.34, and 44.35 m/s. Differences between the two cases are in the delivery radial and velocity errors. The radial error for Case 3 is nearly double that of the linear simulation, yet the standard deviation for the velocity error is the same. Table 7 compares the

unoptimized Monte Carlo simulations for Case 5. The total maneuver ΔV aggregate statistics are comparable. Case 5 is seen to be less sensitive to non-linearity, and so its radial delivery 1-σ error to the target is relatively low at 110 meters (compared to 210 meters for Case 3). The position error (Δp), not shown in the table, is 450 meters, making this delivery accurate even with tight bounds. Comparing the linear and nonlinear deliveries, the velocity is only off by 0.01 m/s, but the error is significantly smaller. This could be due to the tight bounds not limiting the non-linear case as the solution is already relatively accurate.

Table 6: Unoptimized maneuver statistics comparison for Case 3 - AL-Retrograde.

Mnvr.	Linear Monte Carlo					Non-Linear Monte Carlo				
	Mean	1-σ	99%	Radial Err.	Velocity Err.	Mean.	1-σ	99%	Radial Err.	Velocity Err.
	(m/s)	(m/s)	(m/s)	1-σ (km)	1-σ (m/s)	(m/s)	(m/s)	(m/s)	1-σ (km)	1-σ (m/s)
ΔV_1	1.46	0.83	3.94	9.49	0.83	1.56	0.97	4.63	17.63	2.62
ΔV_2	1.35	0.97	4.22	15.70	0.97	1.35	0.97	4.21	22.09	3.49
ΔV_3	0.90	0.49	2.32	5.76	0.49	0.91	0.50	2.34	14.88	9.78
ΔV_4	5.44	3.22	14.81	16.78	3.22	5.56	3.38	15.67	14.33	0.56
ΔV_5	0.86	0.81	3.83	2.43	0.81	0.88	0.85	4.19	1.10	0.59
ΔV_6	1.92	1.96	9.24	3.51	1.96	1.97	2.05	10.27	6.23	0.13
ΔV_7	0.31	0.41	2.19	0.43	0.41	0.32	0.44	2.11	0.34	0.12
ΔV_8	0.20	0.23	1.21	0.13	0.23	0.19	0.19	0.95	0.21	0.23
Total	12.44	8.91	41.76			12.74	9.34	44.35		

Table 7: Unoptimized maneuver statistics comparison for Case 5 - L_2Liss-Prograde.

Mnvr.	Linear Monte Carlo					Non-Linear Monte Carlo				
	Mean	1-σ	99%	Radial Err.	Velocity Err.	Mean.	1-σ	99%	Radial Err.	Velocity Err.
	(m/s)	(m/s)	(m/s)	1-σ (km)	1-σ (m/s)	(m/s)	(m/s)	(m/s)	1-σ (km)	1-σ (m/s)
ΔV_1	2.26	1.18	5.57	13.57	1.18	2.31	1.24	5.82	18.81	2.68
ΔV_2	1.32	0.99	4.26	15.40	0.99	1.33	1.00	4.34	21.61	5.59
ΔV_3	0.39	0.23	1.11	3.05	0.23	0.40	0.23	1.11	37.02	7.68
ΔV_4	3.52	1.92	9.34	2.78	1.92	3.56	1.96	9.28	6.69	0.42
ΔV_5	1.03	0.57	2.76	0.61	0.57	1.04	0.59	2.90	8.18	0.44
ΔV_6	0.54	0.35	1.74	0.45	0.35	0.55	0.37	1.82	1.47	0.13
ΔV_7	0.18	0.11	0.52	0.23	0.11	0.18	0.11	0.54	2.17	0.09
ΔV_8	0.16	0.12	0.54	0.45	0.12	0.16	0.12	0.55	0.11	0.11
Total	9.41	5.45	25.84			9.53	5.63	26.35		

Optimized Nonlinear Cases

Each case is optimized nonlinearly to reduce the total ΔV and improve the delivery to arrival. Mass changes due to burns was not considered in this investigation. Maneuver magnitudes and directions are unconstrained, but the burn epoch is fixed. Maneuvers target the position or velocity at the next ΔV's epoch, and the final one targets the arrival position coordinates. If these maneuvers are not optimized together, the resulting total ΔV can be large, and so maneuver chains can be created to jointly optimize a set of them at the expense of slightly modified arrival conditions. Target bounds can be opened up in portions of the trajectory that do not require a precise delivery like during the resonant orbit portion (maneuvers 1-3). This enables the optimizer to reduce the ΔV while still maintaining a flyable trajectory.

Across all cases, the largest two burns are maneuvers 2 and 4 which occur during the resonant orbit portion of the endgame trajectory and the transition to the final approach. ΔV_4 is the largest, and this is attributed to the increased delivery precision required before beginning the low energy capture at Europa. The target bounds were opened up to 5 kilometers for this maneuver to reduce the ΔV without compromising maneuver cost downstream. For each case, the bounds for ΔV_5

16

and ΔV_6 were reduced to 2 kilometers and ΔV_7 to 1 kilometer if the case has a 8 total statistical maneuvers. The final delivery bounds were set to 0.5 km. Case 1, summarized in Table 8, has the largest total ΔV of all the cases. 2 samples (0.04% of the total) were discarded from this run. Statistical maneuver 6 is placed at the apoapsis location, and 20 hours later the second to last one is performed. In prior sensitivity analysis, it is seen that state errors grow rapidly roughly 13 hours to 10 hours from landing. Thus, the delivery uncertainty from ΔV_7 to arrival would be too large. An additional ΔV is added 10 hours to arrival. With the additional 1.05 m/s mean maneuver, the radial error standard deviation is 0.65 km.

Table 8: Maneuver Statistics for Case 1 - L_2Liss-Prograde

Mnvr.	Mean. (m/s)	1-σ (m/s)	99% (m/s)	Δp 1-σ (km)	Radial Err. 1-σ (km)	Velocity Err. 1-σ (m/s)
ΔV_1	0.10	0.27	1.3	9.23	17.83	2.59
ΔV_2	1.28	0.97	4.11	15.87	19.85	4.34
ΔV_3	0.14	0.33	1.55	10.73	11.26	6.87
ΔV_4	3.53	2.60	12.75	11.33	6.61	0.57
ΔV_5	0.51	0.41	2.11	9.30	16.88	0.21
ΔV_6	0.87	0.97	4.82	7.39	12.35	0.23
ΔV_7	0.60	0.69	3.44	16.28	22.41	0.80
ΔV_8	1.05	1.62	8.09	2.74	0.65	0.62
Total	8.09	7.87	38.16			

Table 9 summarizes Case 2 which follows a direct prograde orbit to a retrograde landing. Like Case 1, a statistical burn at apoapsis is included as this location yields the lowest position error and has the largest influence on the trajectory downstream. The final burn is added 20 hours to landing. A total mean of 4.92 m/s is required but a majority of this is used for the second and fourth maneuvers which are commonly large across all cases. The position and radial error standard deviation at arrival is 2.44 and 0.23 km respectively. Case 3 had 1 outlier sample omitted from the data set. The trajectory includes a close approach to Europa prior to landing, and maneuvers were placed to avoid this location as the errors grew non-linearly from the sensitivity analysis. ΔV_6 has a larger magnitude and position error which can be attributed the instability around apoapsis. The final statistical burn occurs at a constrained 20 hours from landing, but ΔV_7 can likely be shifted further downstream as it is 22 hours from the last burn. By optimization, the total mean and 99th percentile ΔV is reduced from 12.74 m/s to 6.03 m/s and from 44.35 m/s to 25.11 m/s respectively. The delivery to the arrival point has a slightly improved position error of 2.47 km from 2.60 km from the unoptimized run.

Table 9: Maneuver Statistics for Case 2 - DPO-Retrograde

Mnvr.	Mean. (m/s)	1-σ (m/s)	99% (m/s)	Δp 1-σ (km)	Radial Err. 1-σ (km)	Velocity Err. 1-σ (m/s)
ΔV_1	0.08	0.11	0.43	5.97	10.8	2.84
ΔV_2	1.30	1.04	4.70	20.91	28.46	4.37
ΔV_3	0.03	0.04	0.17	4.15	7.03	5.89
ΔV_4	3.01	1.91	8.41	4.60	3.51	0.33
ΔV_5	0.24	0.16	0.77	0.50	1.50	0.09
ΔV_6	0.13	0.07	0.33	0.38	0.51	0.05
ΔV_7	0.07	0.04	0.18	0.89	0.38	0.05
ΔV_8	0.06	0.05	0.19	2.44	0.23	0.24
Total	4.92	3.41	15.18			

Table 10: Maneuver Statistics for Case 3 - AL-Retrograde

Mnvr.	Mean. (m/s)	1-σ (m/s)	99% (m/s)	Δp 1-σ (km)	Radial Err. 1-σ (km)	Velocity Err. 1-σ (m/s)
ΔV_1	0.09	0.22	0.93	9.10	18.14	2.56
ΔV_2	1.32	1.04	4.67	15.67	20.98	2.74
ΔV_3	0.05	0.11	0.61	9.77	12.10	6.49
ΔV_4	3.29	2.43	11.61	9.98	9.98	0.40
ΔV_5	0.35	0.40	1.94	1.02	1.93	0.53
ΔV_6	0.73	0.78	4.17	1.43	2.54	0.09
ΔV_7	0.14	0.16	0.79	0.24	0.50	0.11
ΔV_8	0.07	0.08	0.36	2.47	0.42	0.48
Total	6.03	5.23	25.11			

Case 4 is outlined in Table 11. The same position targeting strategy from all the presented cases is employed in this run with maneuvers 5-7 being chained together with a maneuver cost reduction optimization. The mean ΔV is only 4.8 m/s with a delivery position error of 1.75 km. Additionally, Case 4 was modified to study the effects of velocity targeting. This was initially considered for the resonant orbit and final approach portion of the trajectory. In testing, this method reduced the ΔV at the specific maneuver, but maneuvers downstream had significantly larger ΔVs. When Case 4 was optimized to have maneuvers 1-3 target velocity while 4-8 target position, the magnitude of ΔV_4 was greater than 30 m/s, essentially making the trajectory unfeasible. Alternatively, another version was created to target position for maneuvers 1-3, have maneuver 4 target velocity (in attempt to reduce the ΔV), and have 5-8 target position coordinates. This version has ΔV_4 reduce to 0.0 m/s, but ΔV 5 and 6 increased to a mean of 8.2 m/s and 4.6 m/s respectively. The total ΔV increased to 14.4 m/s compared to the nominal case of 4.8 m/s. In essence, velocity targeting reduced the current burn to 0.0 m/s at the expense of maneuvers downstream, thus shifting where the most expensive maneuver(s) is in these trajectories. Case 5 has the best overall performance with a mean of 5.73 m/s and a position delivery σ of 470 meters. Case 1 and 5 are similar, but case 1 has an additional apoapsis event which increases the positional errors just before landing. This in turn makes the final two maneuvers larger in magnitude than Case 5 (0.6 and 1.05 m/s as opposed to 0.13 and 0.17 m/s). Overall, the good performance of this trajectory is expected as the sensitivity study predicts this behavior. When comparing the optimized to the unoptimized version in Table 7, it is seen that the total ΔV is roughly halved. This reduction only comes from the resonant orbit portion of the trajectory though. For the final approach, the values are roughly similar despite a chain optimization. The radial error standard deviation is comparable, but the velocity error is reduced by 0.37 m/s.

Table 11: Maneuver Statistics for Case 4 - 1 Loop-Retrograde

Mnvr.	Mean. (m/s)	1-σ (m/s)	99% (m/s)	Δp 1-σ (km)	Radial Err. 1-σ (km)	Velocity Err. 1-σ (m/s)
ΔV_1	0.17	0.44	2.31	9.67	19.44	2.58
ΔV_2	1.36	1.06	4.54	15.59	20.7	3.59
ΔV_3	0.03	0.04	0.16	13.42	18.25	6.29
ΔV_4	2.75	1.98	9.82	3.50	3.44	0.33
ΔV_5	0.35	0.21	1.12	0.45	1.32	0.11
ΔV_6	0.12	0.06	0.30	0.31	0.51	0.05
ΔV_7	0.03	0.02	0.09	1.75	0.17	0.20
Total	4.8	3.8	18.34			

18

Table 12: Maneuver Statistics Case 5 - L_2Liss-Prograde

Mnvr.	Mean. (m/s)	1-σ (m/s)	99% (m/s)	Δp 1-σ (km)	Radial Err. 1-σ (km)	Velocity Err. 1-σ (m/s)
ΔV_1	0.16	0.36	1.76	9.51	18.38	2.62
ΔV_2	1.29	1.00	4.28	15.55	19.41	4.28
ΔV_3	0.03	0.03	0.16	20.94	29.04	6.18
ΔV_4	2.46	1.61	7.77	7.80	8.51	0.60
ΔV_5	0.92	0.43	2.39	3.68	6.27	0.46
ΔV_6	0.56	0.28	1.61	1.34	1.16	0.10
ΔV_7	0.13	0.08	0.41	1.48	2.49	0.11
ΔV_8	0.19	0.12	0.54	0.47	0.11	0.12
Total	5.74	3.93	18.92			

Sensitivities to Maneuver Execution Errors

A parametric study was conducted by varying the maneuver execution model. A base-case with no execution error was also run for maneuver corrections with respect to state errors only. The Gates error model, outlined in Table 5, is then halved and doubled. Table 13 consists of each case's total mean and 1-σ ΔV statistics. Case 1 appears to be the most sensitive to maneuver execution as its total roughly doubles in magnitude from the half to double runs. Large differences between the none and nominal case suggest that it is the most sensitive from the rest of the candidates. When running the double case a total of 49 outliers (0.98% of the total) were omitted. Cases 2 and 4 performed as predicted with a growth in ΔV as the execution errors grew. Case 5's half error has a smaller mean than the no error case. This is likely due to the sample set generated for this particular run, as the standard deviation is larger than the no error case by 0.06 m/s. The relatively small fluctuation between models implies that the trajectory is less sensitive to maneuver execution errors.

Table 13: Total ΔV Sensitivities to Maneuver Execution Errors for Cases 1-5

Case	Case 1 L_2Liss Prograde		Case 2 DPO-Retrograde		Case 3 AL-Retrograde		Case 4 1 Loop-Retrograde		Case 5 L_2Liss Prograde	
Gates Error	Mean (m/s)	1-σ (m/s)	Mean (m/s)	1-σ (m/s)	Mean (m/s)	1-σ (m/s)	Mean (m/s)	1-σ (m/s)	Mean (m/s)	1-σ (m/s)
None	6.38	5.09	4.83	3.26	5.45	4.24	4.77	3.71	5.69	3.73
Half	6.87	5.88	4.85	3.31	5.61	4.50	4.77	3.73	5.68	3.79
Nominal	8.09	7.87	4.92	3.41	6.03	5.23	4.80	3.80	5.73	3.93
Double	11.78	13.41	5.16	3.69	7.46	7.77	4.93	3.98	5.96	4.31

CONCLUSION

Low-energy trajectories offer an efficient way for missions to encounter planetary moons. Existing navigational techniques employed on high-energy trajectories need to be validated for these cases. In this research we first reviewed five potential ballistic endgame trajectories to Europa via the L_2 neck region. We show that low-energy trajectories are highly nonlinear and sensitive to state perturbations. Errors reduce near apoapsis making this point an optimal location for a statistical maneuver. Because of trajectory sensitivity, conventional maneuver design techniques, such as having several burns target the same aimpoint, cannot apply for long propagations. Instead, maneuver to maneuver targeting is shown to reduce deviations. The linearity assumption for propagation can also be used if the time between corrections is limited. This duration varies based on where along the trajectory the propagation occurs. Despite only a one kilometer mean deviation 48 hours prior

to arrival, errors in all cases grew significantly with the smallest (from Case 5) being greater than 15 km. As the duration increases, the linear and nonlinear propagated samples begin to differ in velocity distributions despite having similar aggregate statistics. A method to reduce along-track errors and improve the delivery to Europa is presented by constraining the terminal flight path angle instead of the epoch. Time variability from the last statistical maneuver to arrival for the studied cases did not exceed 2 seconds, while minimizing flight path angle and latitude errors. We compare linear and nonlinear Monte Carlo maneuver simulations to show that the linear case underestimates the radial and velocity errors at delivery. Each case is then optimized in the nonlinear simulation tool to reduce total ΔV through the endgame trajectory. Future work includes optimizing maneuver epochs and including state uncertainties from orbit determination errors. We also plan to explore how the ΔV through the endgame cases increases when accounting contingencies for missed maneuvers.

ACKNOWLEDGEMENTS

REFERENCES

[1] S. Hernandez, S. V. Wagner, M. Vaquero, Y. Hahn, P. N. Valerino, F. E. Laipert, M. C. Wong, and P. W. Stumpf, "Cassini Maneuver Experience Through the Last Icy Satellite Targeted Flybys of the Mission," AAS/AIAA *Space Flight Mechanics Meeting, AAS 16-243*, Napa, CA, February 2016.

[2] M. Vaquero, Y. Hahn, P. Stumpf, P. Valerino, S. Wagner, and M. Wong, "Cassini Maneuver Experience for the Fourth Year of the Solstice Mission," 08 2014, 10.2514/6.2014-4348.

[3] S. Ardalan, J. Bordi, N. Bradley, D. Farnocchia, Y. Takahashi, and P. Thompson, "Juno Orbit Determination Experience During First Year at Jupiter," AAS/AIAA *Astrodynamics Specialist Conference, AAS 17-595*, Columbia River Gorge, Stevenson, WA, August 2017.

[4] Z. Tarzi, D. Boone, N. Mastrodemos, S. Nandi, and B. Young, "Orbit Determination Sensitivity Analysis for the Europa Clipper Mission Tour," AAS/AIAA *Space Flight Mechanics Meeting, AAS 19-271*, Maui, HI, January 2019.

[5] R. L. Anderson, S. Campagnola, D. Koh, T. P. McElrath, and R. M. Woollands, "Endgame Design for Europa Lander: Ganymede to Europa Approach," AAS/AIAA *Astrodynamics Specialist Conference, AAS 19-745*, Portland, ME, August 2019.

[6] S. Hernandez, R. L. Restrepo, and R. L. Anderson, "Connecting Resonant Trajectories to a Europa Capture through Lissajous Staging Orbits," AAS/AIAA *Space Flight Mechanics Meeting, AAS 19-455*, Maui, HI, January 2019.

[7] S. Hernandez, R. L. Anderson, D. Roth, Y. Takahashi, and T. P. McElrath, "Navigating Low-Energy Trajectories to Land on the Surface of Europa," AAS/AIAA *Space Flight Mechanics Meeting, AAS 21-360*, Virtual, February 2021.

[8] R. L. Anderson, S. Campagnola, and G. Lantoine, "Broad Search for Unstable Resonant Orbits in the Planar Circular Restricted Three-Body Problem," *Celestial Mechanics and Dynamical Astronomy*, Vol. 124, February 2016, pp. 177–199.

[9] R. L. Restrepo, R. P. Russell, M. Lo, and T. P. McElrath, "Europa Lander Trajectory Design Using Lissajous Staging Oribts," AAS/AIAA *Astrodynamics Specialist Conference, AAS 18-491*, Snowbird, UT, August 2018.

[10] E. H. Maize, "Linear statistical analysis of maneuver optimization techniques," *Astrodynamics 1987*, Jan. 1988, pp. 1005–1022.

[11] P. N. Valerino, B. Buffington, K. Criddle, Y. Hahn, R. Ionasescu, J. A. Kangas, T. Martin-Mur, R. B. Roncoli, and J. A. Sims, *Preliminary Maneuver Analysis for the Europa Clipper Multiple-Flyby Mission*, 10.2514/6.2014-4461.

[12] S. V. Wagner and T. D. Goodson, "Execution-Error Modeling and Analysis of the Cassini-Huygens Spacecraft Through 2007," *Spaceflight mechanics 2008 : proceedings of the AAS/AIAA Space Flight Mechanics Meeting*, Galveston, Texas, January 27-31 2008. AAS 08-113.